Dynamic Myocardial Ultrasound Localization Angiography

Philippe Cormier, Jonathan Porée, *Member, IEEE*, Chloé Bourquin, and Jean Provost, *Member, IEEE*

***Abstract*— Dynamic Myocardial Ultrasound Localization Angiography (MULA) is an ultrasound-based imaging modality destined to enhance the diagnosis and treatment monitoring of coronary pathologies. Current diagnosis methods of coronary artery disease focus on the observation of vessel narrowing in the coronary vasculature to assess the organ's condition. However, we would strongly benefit from mapping and measuring flow from intramyocardial arterioles and capillaries as they are the direct vehicle of the myocardium blood income. With the advent of ultrafast ultrasound scanners, imaging modalities based on the localization and tracking of injected microbubbles allow for the subwavelength resolution imaging of an organ's vasculature. Yet, the application of these vascular imaging modalities relies on an accumulation of cine loops of a region of interest undergoing no or minimal tissue motion. This work introduces the MULA framework that combines 1) the mapping of the dynamics of the microvascular flow using an ultrasound sequence triggered by the electrocardiogram with a 2) novel Lagrangian beamformer based on non-rigid motion registration algorithm to form images directly in the myocardium's material coordinates and thus correcting for the large myocardial motion and deformation. Specifically, we show that this framework enables the non-invasive imaging of the angioarchitecture and dynamics of intramyocardial flow in vessels as small as a few tens of microns in the rat's beating heart in vivo.**

Manuscript received May 3, 2021; accepted May 29, 2021. Date of publication June 4, 2021; date of current version November 30, 2021. This work was supported in part by the Fonds Québécois de Recherche Nature et Technologies (FRQNT) under Grant 268556, in part by the Canada Foundation for Innovation under Grant 38095, and in part by the IVADO through the Canada First Research Excellence Fund (Apogee/CFREF). The work of Jonathan Porée was supported in part by the IVADO through the Canada First Research Excellence Fund (Apogee/CFREF) and in part by the Transmedtech Institute through the Canada First Research Excellence Fund (Apogee/CFREF). The work of Chloé Bourquin was supported in part by the Transmedtech Institute through the Canada First Research Excellence Fund (Apogee/CFREF), in part by the FRQNT, in part by the Quebec Bio-imaging Network, and in part by the IVADO through the Canada First Research Excellence Fund (Apogee/CFREF). *(Corresponding author: Jean Provost.)*

This work involved human subjects or animals in its research. Approval of all ethical and experimental procedures and protocols was granted by the Animal Research Ethics Committee of the Montreal Heart Institute under Application 2018-32-03.

Philippe Cormier, Jonathan Porée, and Chloé Bourquin are with the Department of Engineering Physics, Polytechnique Montréal, Montréal, QC H3T 1J4, Canada (e-mail: philippe.cormier@polymtl.ca; jonathan.poree@polymtl.ca; chloe.bourquin@polymtl.ca).

Jean Provost is with the Department of Engineering Physics, Polytechnique Montréal, Montréal, QC H3T 1J4, Canada, and also with the Montreal Heart Institute, Montreal, QC H1T 1C8, Canada (e-mail: jean.provost@polymtl.ca).

This article has supplementary downloadable material available at https://doi.org/10.1109/TMI.2021.3086115, provided by the authors.

Digital Object Identifier 10.1109/TMI.2021.3086115

***Index Terms*— Ultrasound imaging, cardiology, localization microscopy, motion correction, myocardial angiography.**

I. Introduction

IN PATIENTS with known or suspected coronary artery disease (CAD), cardiac imaging tests often constitute the first step in diagnosis and treatment planning. The most typical approach in characterizing CAD focuses on the anatomy of a coronary artery tree by determining which arteries undergo narrowing or obstruction using standard angiography [1]. However, the observed narrowing does not always correlate well with blood flow [2] and heart function or, more importantly, with the patient's symptoms and prognosis [3]. The heart's arterial system is composed of three different compartments of dimensionally distinctive vessels having various functions. The large epicardial coronary arteries ($\sim$ 500 μm to $\sim$ 5 mm) have a capacitance function and flow is subject to little resistance. The intramyocardial vessels, prearterioles ($\sim$ 100 μm to 500 μm) and arterioles ($<$ 100 μm), have respective functions of pressure regulation and metabolic regulation of the myocardial blood flow (MBF) [4]. These structures host the coronary microcirculation and compose the site of coronary microvascular dysfunction (CMD). In the last two decades, this condition has emerged as an important mechanism of myocardial ischemia with a high prevalence in patients with suspected CAD [4]. Guidelines regarding the management of stable CAD now consider atherosclerotic narrowing and CMD through its diagnostic and prognostic recommendations [5]. Furthermore, since coronary angiography is often insufficient to prescribe a percutaneous coronary intervention, clinical practice also relies on fractional flow reserve (FFR) [6] or coronary flow reserve (CFR) measurements to assess the myocardial ischemia risk. However, these measurements can be discordant for around 30 % of intermediate stenosis [3]. Despite the increasing focus on the myocardium's vasculature, no technique can directly visualize the coronary microcirculation in vivo in humans [4], [7]. Ultrasound techniques, based on contrast agents to achieve optimal opacification of the left ventricle, also deliver information on myocardial perfusion but are yet only used in emergency conditions [8]. Moreover, multiple imaging approaches often based on large fixed infrastructure have been developed to obtain diagnostic and prognostic information non-invasively and through indirect measures. However, they often suffer

from limitations in terms of sensitivity and specificity, which may lead, on the one side, to an unnecessary coronary angioplasty or, on the other side, to untreated life-threatening conditions. The advent of Ultrafast ultrasound [9] paired with the capability to accumulate large datasets has recently opened the way for various novel ultrasound-based imaging modes. By transmitting plane waves rather than focused beams, frame rates rose from 50 to 20 000 images per second. For instance, Ultrafast Doppler Angiography has enabled the mapping of large intramyocardial vessels (few hundreds of micrometers in diameter) in the beating heart [10]–[13]. In organs undergoing minimal or no tissue motion, Ultrasound Localization Microsocopy (ULM) [14] has recently enabled the mapping of vessels of a few microns in diameter. However, Ultrafast Doppler Angiography is not sufficiently resolved to investigate smaller intramyocardial compartments, and the complex heart motion limits the implementation of ULM for cardiac imaging. ULM consists of locating and tracking highly echogenic, individual microbubbles within the vasculature. It overcomes the diffraction limit and enables sub-wavelength resolution of vascular pathways [14]. An important tradeoff in ULM is that the gain in spatial resolution is done at the cost of degraded temporal resolution as several minutes are required to fill the vascular network of an entire region of interest. While various microvascular structures like the brain [14], kidney [15], liver [16] and tumors [17], [18] have already been subjects to ULM in vivo studies [19], the heart, which is the target of this study, represents a peculiar challenge due to its fast and high amplitude non-rigid motion. Ultrafast ultrasound is particularly well suited to accurately map and correct for the large motion of the heart. This process is typically based on radiofrequency cross-correlation [20], speckle tracking [21], optical flow [22], [23] or tissue doppler [24], [25].

From a continuum mechanics perspective, motion correction and suppression requires the evaluation and tracking of material points (i.e., Lagrangian coordinates) through time in place of the Eulerian coordinates on which ultrasound images are usually acquired [26]. Such Lagrangian coordinates were used previously for instance in the context of myocardial elastography [27], [28].

Herein, we demonstrate the feasibility of Dynamic Myocardial Ultrasound Localization Angiography (MULA) to assess the myocardium's microvasculature, from coronaries to bigger arterioles, and their dynamic flow behavior in the rat's beating heart in vivo. The development of this novel imaging modality resides on specific methods to adapt the ULM scheme to the cardiac context. Using ECG-gated sequences along with a novel Lagrangian beamformer, we accumulate microbubble events directly in the material coordinates, which enables the subwavelength heart perfusion dynamics visualization within the myocardial wall.

II. Methods

A. Experimental Procedure

This study was performed in accordance with the Animal Research Ethics Committee of the Montreal Heart Institute (Permit: 2018-32-03). 3 Sprague-Dawley anesthetized rats (1,5-2,5 % isoflurane) with depilated chests were placed on a monitoring platform (LabeoTech, CA) in a supine position to acquire ultrasound images. To minimize global displacements, fixed foam stabilizers were positioned in the periphery of the thorax. After injection of a single 10-μL bolus ($\sim 1.2 \times 10^8$) of Definity microbubbles (Lantheus, USA) and a 50 μL saline flush, an ultrasound sequence was launched using a Vantage imaging system (Verasonics, USA) and a L22-14 probe (Vermon, France).

B. Dynamic MULA

The proposed method relies on novel solutions to reduce motion artefacts in the ULM process [16], [29] and enable dynamic imaging of microvessels' blood flow. First, we acquire ultrasound images by successive ECG-triggered time ensembles, which are compatible in the referential of the ECG signal. Images are reconstructed through a Lagrangian beamformer, which corrects for the large non-rigid motion before tissue filtering and microbubble localization. Microbubble positions are then accumulated in a 2D+t microbubble density matrix to generate a subwavelength resolved cine-loop showing the flow dynamics of the vessels and microvessels contained in the field of view through time.

1) Ultrasound Sequence: A compound plane wave sequence of 3 angles ($-3°$ to $3°$) was used to acquire 800 continuous groups of 1200 images at 3000 fps (i.e., 400-ms-long windows with a pulse repetition frequency of 9000 Hz) triggered at the ECG's R-wave during a period approximately 12 minutes long (Fig. 1(a)). Each ensemble of 1200 images covering approximately 2.5 heartbeats was acquired after a minimal pause of 800 ms (the exact duration of the pause was determined by the following trigger signal from the ECG). This minimal pause was implemented according to data transfer constraints. We use the quarter wavelength sampling of the Verasonics system to limit the data transfer bandwidth. The central frequency and sampling frequency after quarter wavelength sampling were set to 15.625 MHz. The imaging was produced with a mechanical index of approximately 0.217.

2) Lagrangian Beamformer: The Lagrangian beamformer was here introduced as means of reducing blurring artefacts and microbubble localization errors associated with large myocardial motion. In most ultrasound applications, beamforming is performed using a standard delay-and-sum (DAS) algorithm [30]:

$$S\left(\vec{x}\right) = \int RF\left(\vec{x}_1, \tau\left(\vec{x}_1, \vec{x}\right)\right) d\vec{x}_1 \tag{1}$$

where $\vec{x} = \{x, z\}$ are the Eulerian coordinates of the pixels within the field of view, $\vec{x}_1$ are the coordinates of the elements of the probe and $\tau\left(\vec{x}_1, \vec{x}\right)$ is the transmit-receive time of flight of the wave front. Because we aim at recovering microvessel positions in the myocardium coordinate system (i.e., as opposed to the probe coordinate system) we introduce a Lagrangian beamformer that can form ultrasound images in the myocardium Lagrangian (or, material) coordinates:

$$S_{Lag}\left(\vec{x}_{Lag}\right) = \int RF\left(\vec{x}_1, \tau\left(\vec{x}_1, \vec{x}_{Lag}\right)\right) d\vec{x}_1 \tag{2}$$

where $\vec{x}_{Lag} = \left\{x_{Lag}\left(x, z, t\right), z_{Lag}\left(x, z, t\right)\right\}$ are the Lagrangian coordinates of the myocardium as a function

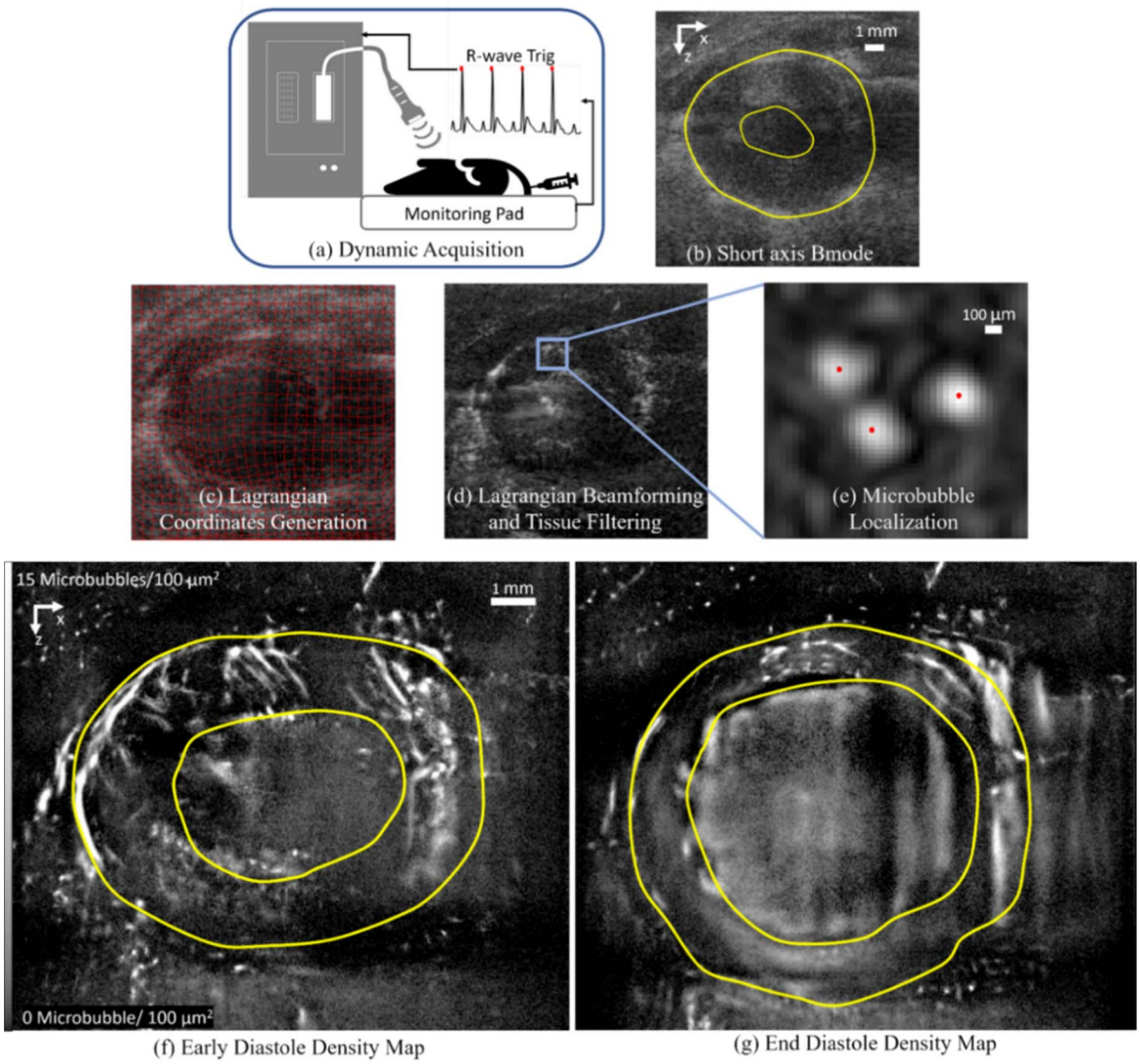

Fig. 1. Dynamic MULA framework. Dynamic acquisition procedure of ultrasound images: (a) Trigger signals are generated from the animal's ECG to drive the ultrasound system. (b) DAS beamformed images of the left ventricle in parasternal short axis view in the systolic period in brightness mode (Bmode, grayscale), overlaid with a manually performed yellow segmentation of the endocardium and epicardium based on B-mode images. (c) Lagrangian coordinates of the diastolic period are shown as a red grid overlaid on the Bmode image. (d) Lagrangian beamformed images were processed through a time-dependent SVD filter to isolate the microbubble signal. (e) A 2D point spread function kernel was correlated with the filtered images followed by a 2D gaussian peak fitting to localize microbubble centroids. Microbubble centroids were accumulated in 17 ms sliding windows to create density maps in early (f) and end (g) diastole.

of space and time. Lagrangian coordinates were evaluated using a regularized framework that can map the Lagrangian coordinates of the tissue from its velocity vector measurements $\vec{v}_T(\vec{x})$. It can be defined as follows:

$$\vec{x}_{Lag} = \underset{\vec{x}}{\operatorname{argmin}} \left\{ \left\| \frac{d\vec{x}}{dt} - \vec{v}_T(\vec{x}) \right\|^2 \right\} \tag{3}$$

where the tissue velocity vectors $\vec{v}_T(\vec{x})$ can be evaluated from tissue Doppler measurements (see the following sections). Since $\vec{x}$ is non-regular, (3) must be evaluated iteratively as it requires the evaluation of $\vec{v}_T$ at $\vec{x}$ that is, at first unknown. To do so, we first initialize the Lagrangian coordinates as the Eulerian coordinates:

$$\vec{x}^0_{Lag} = \vec{x}_{Euler} \tag{4}$$

and iteratively search for the Lagrangian coordinates using:

$$\vec{x}^i_{Lag} = \underset{\vec{x}}{\operatorname{argmin}} \left\{ \left\| \vec{x} - \vec{x}_{Euler} + \int_{t_{ref}}^{t} \vec{v}_T(\vec{x}^{i-1}_{Lag}, t)dt \right\|^2 \right\} \tag{5}$$

where t_{ref} is the reference time from which the Lagrangian coordinates evolves (i.e., at $t = t_{ref}$ we have $\vec{x}_{Lag} = \vec{x}_{Euler}$) and t is defined from the beginning to the end of the cine-loop duration. t_{ref} was chosen as the peak systole to maximize the myocardium's area transverse to the imaging field in the reference frame.

In practice, we first evaluated the regularized tissue vector field $\vec{v}_{Tissue}$ using directional Color Doppler [31] as detailed in the following subsections.

a) Tissue doppler measurement: Following in-phase quadrature (IQ) demodulation of the raw RF signals and DAS

beamforming (Fig. 1(b)), we proceeded to a multi-receive-angle (−5°, 0°, 5°) autocorrelation technique to retrieve directional Doppler shift measurements ϕ_N [32]. Phase shifts were converted to Doppler velocities as follows:

$$V_{D_N} = \frac{\lambda f_r \phi_N}{4\pi} \tag{6}$$

where V_{D_N} is the N$^{\text{th}}$ angle Doppler velocity, λ is the emission wavelength and f_r is the frame rate. Autocorrelation was also used to formulate a weighting function:

$$\omega_{D_N} = \frac{|R_N(1)|}{R_N(0)} \tag{7}$$

Here $R_N(1)$ and $R_N(0)$ are the lag one and lag zero complex autocorrelations for the N$^{\text{th}}$ receive angle, respectively. In practice, this weighting function was set to 0 for values under 0.75 and the autocorrelation was performed on a temporal packet size of 4. Both these parameters were chosen following an iterative approach to minimize the effects of blood within the ventricle's cavity on the regularization while maintaining a visually coherent estimation of motion.

The next operations describe how the tissue velocity field $\vec{v}_T = \{v_x, v_z\}$ was retrieved from Doppler velocity measurements. To alleviate Doppler noise and outliers, we adopted a spatiotemporal vector regularization framework. For numerical considerations, we separated spatial (see section B.2.b) and temporal regularizations (see section B.2.c).

b) Spatial regularization: Here we refer to the spatially regularized velocity field as $\vec{v}_s$, which was found by solving the following minimization problem:

$$\vec{v}_s = \underset{\vec{v}}{\text{argmin}} \{J_D(\vec{v}) + \alpha_s J_{TPS}(\vec{v})\} \tag{8}$$

where α_s is used to balance the smoothing $J_{TPS}(\vec{v})$ and data fitting $J_D(\vec{v})$ of the function. $J_D(\vec{v})$ corresponds to the error term between the Doppler measurements and the vector velocity projection onto the Doppler axis. It is defined as follows:

$$J_D(\vec{v}) = \sum_{\theta_N} \int_{\Omega,t} \omega_{D_N} \left(\vec{d}_{D_N}.\vec{v} - V_{D_N}\right)^2 \tag{9}$$

where $\vec{d}_{D_N}$ is a unit vector describing the Doppler orientation [25], Ω is the domain of interest, which includes the entire heart, and θ_N are the selected Doppler orientations.

To ensure the spatial continuity of the velocity field, and hence the spatial continuity of the Lagrangian coordinates we used a thin plate spline constraint [33], defined as:

$$J_{TPS}(\vec{v}) = \sum_{i=\{x,z\}} \int_{\Omega,t} (\partial_{xx} v_i)^2 + 2(\partial_{xz} v_i)^2 + (\partial_{zz} v_i)^2 \tag{10}$$

c) Temporal regularization: To ensure the temporal continuity of the velocity field and prevent drifting artefacts [34], we introduced a temporal constraint that is the weighted sum of the first order temporal derivative and a periodic derivative. It was defined as follows:

$$J_{regt}(\vec{v}) = \alpha_t \int_{\Omega,t} \|\partial_t \vec{v}\|^2 + \alpha_T \int_{\Omega,t} \|\partial_T \vec{v}\|^2 \tag{11}$$

where ∂_t is a temporal derivative operator and ∂_T a periodic derivative operator computing the slope between an instant and its periodic following, which in this study corresponds to the heartbeat period (i.e., $T = 1/HeartRate$) hence enforcing the velocity field to be reproducible between heartbeats. α_t and α_T coefficients were respectively chosen to weight the temporal and periodic smoothing.

The spatiotemporal regularized vector velocity field $\vec{v}_{st}$ was found by solving the following minimization problem:

$$\vec{v}_{st} = \underset{\vec{v}}{\text{argmin}} \left\{ \int_{\Omega,t} \omega_D \left\|\vec{v} - \vec{v}_s\right\|^2 + J_{regt}(\vec{v}) \right\} \tag{12}$$

where ω_D is the Doppler autocorrelation weighting function ω_{D_N} averaged over Doppler orientations and $\vec{v}_s$ is the spatially regularized vector velocity field found in section A.2.b).

d) Lagrangian coordinates generation: The following step was used to convert velocity fields into Lagrangian coordinates by integration as a solution of the equation (3). The key concept here was to implement motion within the imaging plane's mesh (Fig. 1(c)). This mesh was initialized as a Eulerian grid whose origin was set at the center of the aperture. The mesh was then updated iteratively using (5). In practice, a first subset of 20 ensembles of 1200 images acquired before the microbubble injection was processed through a Eulerian beamformer to generate the Lagrangian coordinates. The remaining ensembles were then processed with the Lagrangian beamformer.

e) Algorithm implementation: Approximate solutions to the minimization problems described in (8) and (12) were computed over a cartesian grid as described in previous studies [25], [35]. The algorithm was implemented through the following steps:

1. Retrieve Doppler velocities, directions and weighting functions through autocorrelation (see section B.2.a).
2. Build vectors and matrix operators for the numerical representation of the functionals (see [25] section III.B.).
3. Solve the spatial regularization least squares problem (8).
4. Solve temporal regularization least squares problem (12).
5. Compute Lagrangian coordinates $\vec{x}^i_{Lag}$
6. Evaluate Doppler Velocities and directions in Lagrangian coordinates (i.e., $V_{D_N}\left(\vec{x}^i_{Lag}, t\right)$)
7. Repeat steps 2-6 to regularize the problem in Lagrangian coordinates.

In practice, Lagrangian coordinates were sufficiently stable after 3 iterations.

3) Localization: Following Lagrangian beamforming, we applied a time-dependent spatiotemporal filter consisting of a 17-ms (or, 50-frame) sliding window SVD (Singular Value Decomposition) filter [10], [19] with an overlap of 25 frames between windows to extract microbubbles, for each image ensemble. The SVD-filtered images were then correlated to a simulated point spread function (PSF) to locate microbubbles based on the 15 MHz linear array parameters using a simulation software. To minimize the noise level in

the localization process, only the subwavelength centroids of the microbubbles with a PSF correlation higher than 0.8 were retrieved using a 2D gaussian fitting of the correlation map local peaks. Cine loops were then generated by accumulating the microbubble centroids within 17-ms sliding temporal windows in a 10-μm spatially resolved microbubble density map (Fig. 1(d)-(g)).

C. Comparison Approach

To evaluate the performance of the proposed Lagrangian method, we also developed two alternatives.

1) Dynamic Angiography Without Motion Correction: To quantify the performance of the Lagrangian beamformer, we also beamformed our data using a conventional Eulerian beamformer. For this approach, the localization process remains the same and no motion correction on the microbubbles is applied.

2) Dynamic Angiography With Motion Correction on the Microbubble Positions: As additional means of comparison, we proposed a second method for motion correction. This alternative technique consists in the modification of the localized microbubble positions $\vec{x}_{MB_t}$, detected after Eulerian beamforming (1), with respect to the measured tissue motion retrieved by our algorithm. Specifically, this approach was used to assess the effect of motion correction when it is applied after beamforming and SVD filtering in comparison to the Lagrangian beamforming. The computation of the motion corrected localizations $\vec{x}_{MB,MoCo_t}$ is made through a similar process as the material coordinates generation. The position of motion corrected microbubbles is given by:

$$\vec{x}_{MB,MoCo_t} = \vec{x}_{MB_t} - \int_{t_{ref}}^{t} \vec{v}_{st}(\vec{x}_{MB_t}, t)dt \tag{13}$$

3) Comparison: The comparison method relies on a vessel profile analysis. This was done by demarcating the same vessel structures in the density maps of each configurations and MULA, then measuring the full width half maximum (FWHM) of the structures.

III. Results

A. Lagrangian Coordinates Generation and Beamforming

Figure 2 displays the Lagrangian coordinates behavior through the heartbeat cine-loop. The coordinates (red grid) are shown to follow a dilation pattern from systole to diastole (Fig. 2(a) and (b)). The blue and green regions of interest (Fig. 2(a)) are used to respectively measure vertical and lateral displacements of the Lagrangian coordinates and are located at a few hundreds of micrometers from the endocardium. Fig. 2 (c) presents the average displacements within the colored regions of interest (ROIs), relative to the reference of the Lagrangian grid (systole period) as a function of time. Peak mean displacement measurements are 490 μm laterally and 480 μm axially. Additionally, the supplementary video 1 shows the dynamic evolution of the Lagrangian coordinates. It enables the visualization of temporal and spatial smoothness

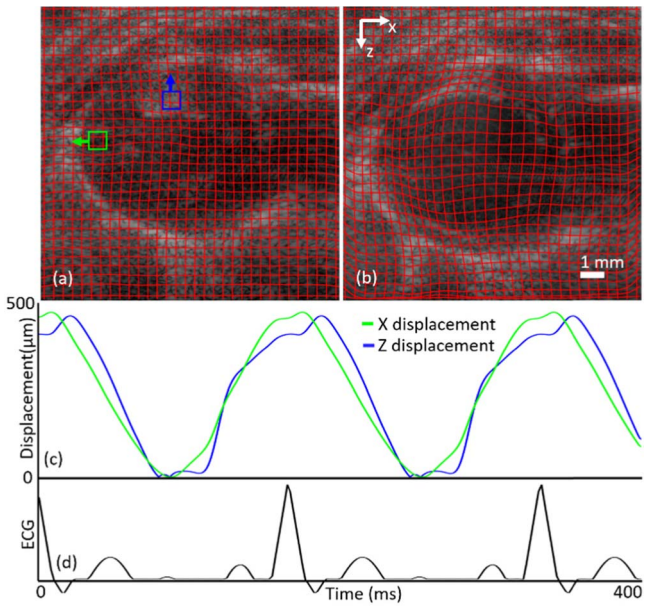

Fig. 2. Myocardial movement tracking through Lagrangian coordinates. Lagrangian coordinates grid (red) overlaid on Bmode images (grayscale) of the left ventricle in the systole period (a) and diastole period (b). (c) Curves of displacement respective to the peak systolic period are shown through the heartbeat cine-loop. (d) Simulated electrocardiogram for illustration purposes.

of the grid, the periodic behavior and the different patterns in the motion: dilation, contraction and rotation. These coordinates are used to generate the Lagrangian beamformed cine loops as displayed in the supplementary video 2.

B. Motion Based Enhancements

To assess the differences between the proposed MULA framework and comparison configurations from section II.C, a line was drawn intersecting vessels emerging from a treelike structure on the microbubble density maps of each comparison configuration in the early diastolic period (Fig. 3(a)-(c)). Three transverse vessel profiles were selected for analysis based on their amplitude and well-defined peaks. Figure 3(d) shows the projection of the density maps on the line for all configurations. For the two largest vessel profiles on the right end of the green line, the MULA approach leads to a FWHM measurement which is 39 % smaller (134 μm to 81 μm) and 28 % smaller (89 μm to 64 μm) with higher peaks than the approach without motion correction. For the third vessel, the scenario without motion correction denotes the smallest FWHM but again with a lower peak. In the case where the positions of microbubbles were corrected (equation (13)), we obtained FWHM measurements of 70 μm, 66 μm and 93 μm.

C. Assessment of the Myocardium's Vasculature

The supplementary video 3 shows the microbubble density cine-loop produced by MULA projected on Eulerian coordinates. The Figure 4 displays snapshots of this cine-loop for the systolic, early diastolic and end diastolic periods. Few tens of vessels were localized within the intramyocardial region. The vessels can be seen pulsing periodically in various regions

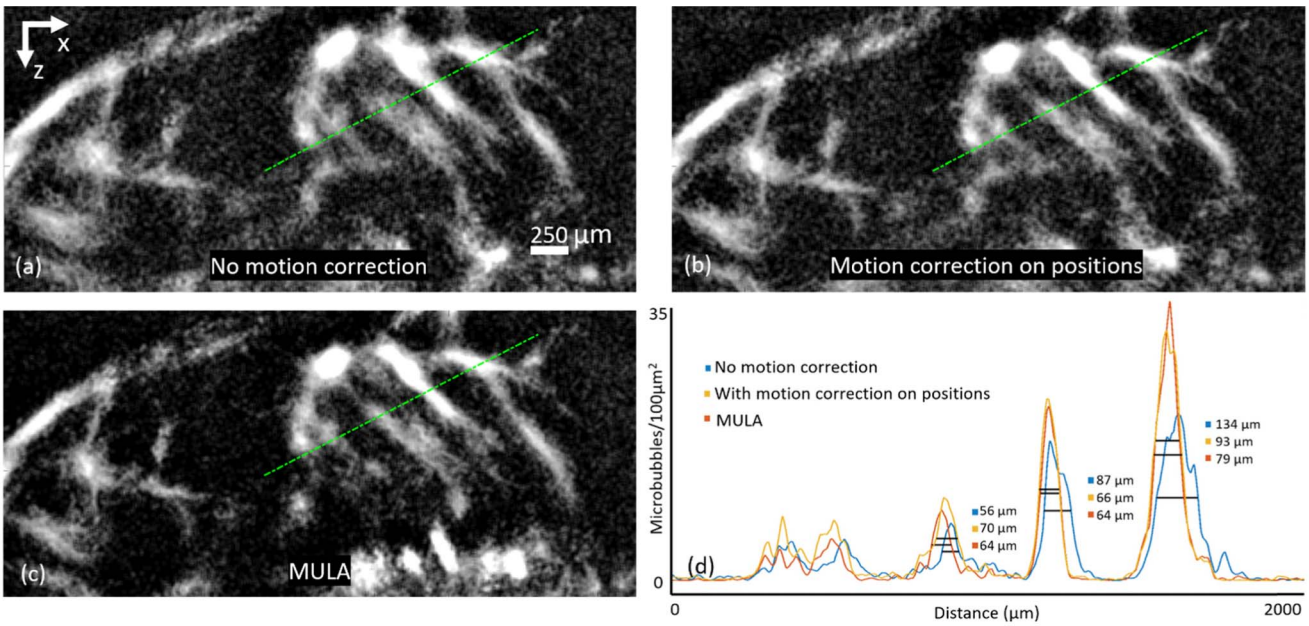

Fig. 3. Microbubble density profiles of vessels in different configurations. (a) DAS beamformed images without any motion correction. (b) Motion correction of the Microbubble positions localized from DAS beamformed images. (c) Dynamic MULA. (d) Microbubble density profiles of the three comparison configurations along the green dotted line with the full width half maximum measurement of three vessel profiles.

of the imaging plane with each heartbeat. The arrangement of these vessels varies through the heart cycle. Globally, few larger vessels are clearly shown emerging from the epicardium and remain discernable through most of the heartbeat. They spread downwards in smaller networks of more numerous vessels crossing the myocardial wall to the endocardium, which are mostly present when the myocardial wall is contracted. The size of the vessels located in the myocardium varied from 60 μm to 200 μm and more of them were discernable in the anterior section of the myocardium (top half of the imaging plane).

In Figure 5, the MULA vascular imaging framework was used to measure dynamic flow parameters of a vessel. The white rectangle in (a) delimits the ROI of the analysis, which is a posterior section of the left ventricle wall. Within the ROI, the 3 sub-regions were color coded to represent a proximal, intermediate and distal portion of a vessel relative to the epicardium (Fig. 5(b)). The image sequence of the ROI is shown at 25 % of the upstroke for each sub regions which are measured by taking 25 % of the microbubble filling peak within the sub-regions. Moreover, the red region includes a proximal large transversal section, the blue region includes the top section of an underlying vessel (intermediate) and the green region includes a deeper portion of the same vessel (distal). The 25 % upstroke timings (black dots in Fig. 5(c)) in the chronological order are the following: 64 ms (proximal), 73 ms (intermediate) and 77 ms (distal) for the first heartbeat of the cine-loop, and 243 ms (proximal), 249 ms (intermediate) and 253 ms (distal) for the second heartbeat of the cine-loop.

IV. Discussion

In this study, we have demonstrated the feasibility of a novel imaging framework called MULA to map blood vessels with subwavelength resolution in presence of large motion within the myocardial wall. The chosen approach of an ECG-gated acquisition paired with a motion correction algorithm, which reduces the heart's non-rigid motion, has enabled the imaging of the angioarchitecture and hemodynamics of the intramyocardial microvasculature. The Lagrangian beamforming was successful at reducing the displacements of the tissue during the entire heart cycle.

A. Measuring Heart Motion

The implementation of the motion registration algorithm was based on numerous parameters and configuration choices. Most of our analysis was made by iterating the smoothing and weighting parameters and observing the velocity fields and material coordinates overlaid on Bmode films (Fig. 2(b), external video). Since the left ventricle cavity was an important portion of the imaging field and had no coherent tissue information due to its blood composition, we have imposed a threshold on the pixelwise weighting parameter to suppress its influence in the algorithm (see equation (7)). The value of the threshold (0.75) was fixed through observations of Doppler measurements of the cavity. The motion and hence the Lagrangian coordinates in these regions of the imaging plane ($\omega_{D_N} < 0.75$) were extrapolated from their neighbors thanks to the global regularization framework (see equations (8)-(12)).

As shown in Figure 2, the reference material coordinates grid was set for the systolic state and the grid follows the contraction and relaxation movements of the heart. Figure 2 shows how the periodicity of the beating heart was well reproduced by our framework. We can also acknowledge that our framework has successfully performed the registration of both axial and lateral tissue motion since the magnitudes are similar, as expected in a short-axis view. The displacements clearly follow the ventricular systolic period, which lasts from the peak of the R-wave to the end of the T-wave, followed

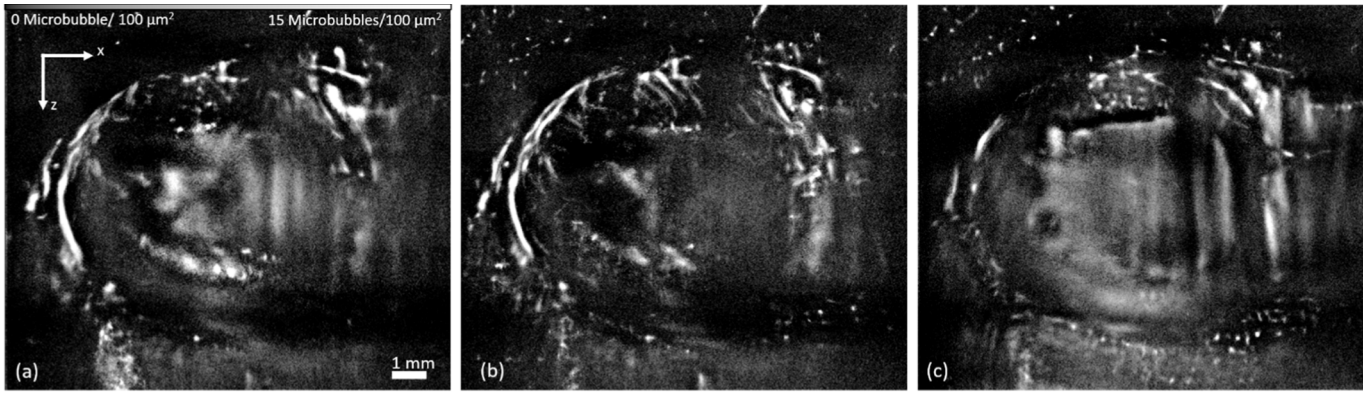

Fig. 4. Cine-loop snapshots of the MULA framework through the heartbeat. (a) The microbubble density map in the systolic period. (b) The microbubble density map in the early diastolic period. (c) The microbubble density map in the end diastolic period.

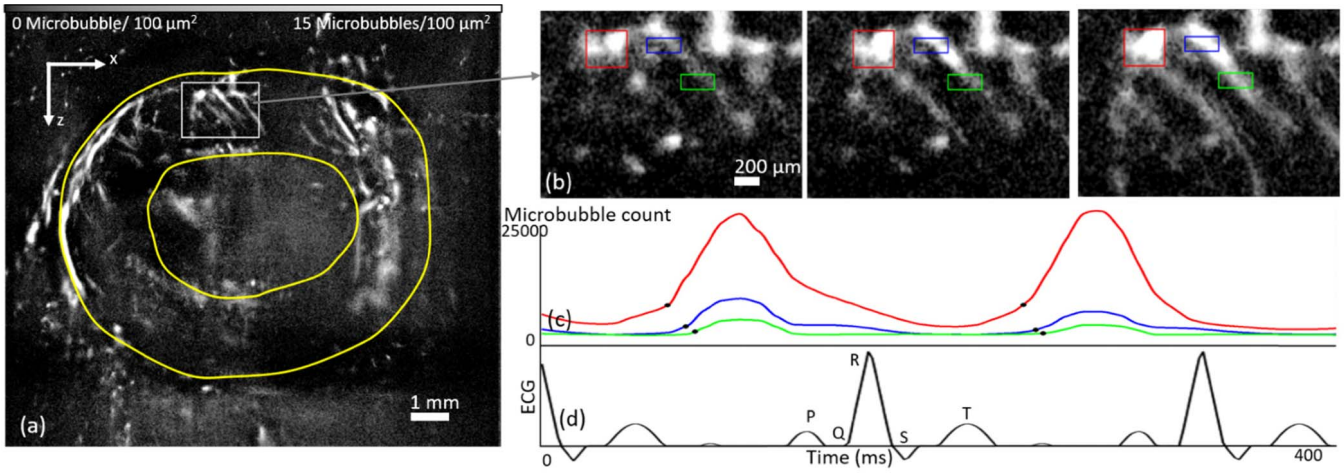

Fig. 5. Dynamic imaging of microbubble perfusion. (a) The microbubble density map in the early diastolic period is overlaid with the segmentation of the endocardium and epicardium (yellow outline), with the region of interest (gray rectangle) for the dynamic analysis. (b) Image sequence of microbubble perfusion of vessels within the region of interest. (c) Color-coded sub regions are represented as the proximal, intermediate, and distal sections of the vessel relative to the epicardium. The three time-samples of the image sequence concord with the 25 % upstroke mark of microbubble filling within the proximal, intermediate and distal sub regions of the first heartbeat of the cine-loop. Dynamic evolution of microbubble density within each sub region of interest through the heartbeat cine-loop with respective 25 % upstroke marks shown in black dots is represented by respectively color-coded curves. (d) Simulated electrocardiogram shown as temporal reference.

by a relaxation period completing the ECG cycle, which is the ventricular diastole. On the displacement's amplitude point of view, our framework has led to peak displacements of 490 μm laterally and 480 μm axially. As means of comparison, we have measured on Bmode images (Fig. 1(b)) the peak-to-peak axial displacement from the contracted to relaxed state, which is approximately 1 mm for the endocardium and 500 μm for the epicardium. Considering the chosen method, temporal and spatial smoothing components must be well dimensioned to ensure a coherent physiological movement of the model but weakens the large amplitude variations. Hence, we concluded that the magnitude of our measurements, which are composed at a few hundreds of μm from the endocardium, are representative of the heart's motion.

B. Improving Vessel Mapping

A key factor of the MULA application resides in the accumulation of the microbubble positions over time. From our analysis of vessel maps without any motion compensation, we came to these observations: 1) The myocardial movement drives the blood vessels to move in space over the heartbeat, which will be inducing large blurring effects when we compound periods of time to build vessel maps. 2) Since the tissue is in motion, implementing a clutter filter based on SVD is challenging due to the similarity in temporal behaviors between the perfusion of microbubbles and the myocardial motion. To assess both these constraints, we have used our Lagrangian beamformer to form cine loops with large motion correction. As shown in the supplementary video 2, the motion of the myocardium through the heartbeat cine loops is efficiently reduced by this process. In parallel, we have analyzed vessel maps where motion correction was applied on the final localization of microbubbles from a standard DAS beamforming. As shown in Figure 3, all configurations are compared for a vessel map formed with 200 frames (which represents approximately 67 ms of the cine-loop) in the early diastole. The resolution of vessels was positively affected by the motion compensation: FWHM of vessels provided by the MULA framework were approximately 30 % smaller than without any motion correction. By performing our comparison method of motion correction on microbubble positions,

we have confirmed that MULA is compensating the motion effects through the Lagrangian beamformer. Also, the results provided by MULA do seem to have a better contrast over the motion correction on positions results, which might be due to the improved tissue filtering of the Lagrangian beamformed images. This might explain why FWHM results coming from MULA were on average 9 % smaller than the alternate motion correction on positions scenario.

For further clinical applications of this modality, we believe that Lagrangian beamforming is the logical path to follow. Being able to compound larger portions of the cardiac cycle to create vessel maps would speed acquisition times, as we could form robust 2D vessel maps with less image ensembles. Yet this would decrease the temporal resolution of the dynamic analysis by reducing the time samples of the 2D+t density matrix. However, obtaining better resolved vessels at this scale through the Lagrangian beamformer can improve the sensibility of the modality and could be investigated as a coronary microvascular dysfunction diagnostic tool. Furthermore, being able to filter efficiently the organ's tissue should help to decrease the time to build well defined vessel maps, since it can improve the contrast to noise ratio. In conclusion, the Lagrangian beamformer has allowed substantial improvements of the vessel cine loops over the cardiac cycle.

C. Assessment of the Myocardium's Vasculature

1) Cardiac Angiography: As shown in supplementary video 3 and in the Figure 4, accumulating the microbubble centroids over short periods of time (i.e., 50 ms) enabled vessels to emerge in various sections of the imaging field. Early moments of the relaxation movement of the heart muscle, corresponding to the early diastolic phase, had higher microbubble concentrations, which can be correlated with flow. Hence, density maps generated from this period had greater information on the angioarchitecture of the myocardium. The range of dimensions of imaged intramyocardial vessels, which goes from 64 μm to 200 μm, correlates with the size of pre-arterioles and arterioles within the myocardial wall. We have also depicted structures as small as 40 μm in diameter resembling vessel patterns which is encouraging for future developments of MULA. This would require further validation. Mostly larger vessels ($\sim$ 200 μm) were detected in the epicardial region, which supports the hypothesis that this region is feeding downward vessel structures within the myocardium aimed towards the left ventricle cavity. This behavior is coherent with the perfusion cycle of the heart where the large epicardial coronary arteries feed the downstream myocardial arterioles and capillaries. For further use of our proposed approach to generate vascular maps, the selection of specific heartbeat periods where vessels look sharper and denser could be considered to make a static angioarchitecture analysis, but it was acknowledged that remaining tissue motion paired with the perfusion behavior of cardiac vessels is challenging the microbubble accumulation process through the complete heartbeat. The dimension of the vessels detected by MULA and their configuration suggest that the proposed method was able to recover the intramyocardial microvasculature.

2) Dynamic Analysis: Adjacent to the ability to image the angioarchitecture of the microvasculature, this study was meant to evaluate MULA's capability to investigate dynamic properties of the intramyocardial blood flow. The dynamic behavior suggesting a perfusion from larger epicardial vessels toward the myocardial microvasculature was also observed in the whole left ventricle wall during the heartbeat cine-loop. We did witness the flow, which was here represented by microbubble density variation, arriving firstly to the epicardium and then propagating to deeper intramyocardial structures (supplementary video 3). Figure 5 confirms this behavior for a well-defined vessel tree: the subregion proximal to the epicardium (red) reaches 25 % of upstroke 9 ms before the intermediate subregion (blue) which is 4 ms before the distal subregion (green). This sequential order is maintained in the second heartbeat of the cine-loop (6 ms proximal-intermediate, 4 ms intermediate-distal) which increased the confidence of these results. We have also witnessed the coherence between the myocardial perfusion and the ECG signal. The ventricular diastole, which goes from the end of the T-wave to the peak of the R-wave, seems to host most of the perfusion of the analyzed intramyocardial ROI. This was expected since the heart starts relaxing in the early diastole where there is a pressure drop in the aorta which allows the perfusion of the coronary vasculature. Intramyocardial vessels are compressed and restrain flow during systole due to high ventricular pressure. They are then subject to lower pressure and are freed of compression during the diastolic period, which allows for perfusion. This demonstrates the capabilities of MULA to image the intramyocardial vasculature dynamically. It also paves the way towards the monitoring of important blood flow biomarkers such as the Coronary Flow Reserve in situ [3] for the diagnostic of cardiovascular pathologies.

D. Limitations

This study has brought to light some limitations of the proposed MULA framework and its performance on the cardiac microvascular imaging of the rat in vivo.

- First, the proposed MULA framework resides in a 2-dimensional approach to a 3-dimensional problem. The use of a linear array probes to form a 2D+t cine-loop will inevitably lead to the presence of out-of-plane motion. The relatively low elevation resolution of linear probes and the presence of out-of-plane motion inevitably impacts the motion correction performance. The adaptation of the MULA framework to 3D echography would lift these limitations and provide further validation of the methodology.
- Portions of the images had reduced signal due to the high echogenicity of either the overlying ribs or the microbubble filled cavity for the posterior myocardial wall. The associated degraded image quality in these regions impacted both tissue motion and microbubble detection, which creates ambiguity as whether a given region is poorly perfused or simply shadowed. A particular example of this observation would be the column area on the right of the region of interest in Fig. 5

which is much less contrasted. We believe that the rib shadowing would be highly reduced in human subjects where ultrasound operators are trained to position the probe in between ribs. Future works should also aim at lower microbubble concentrations to lower the impact of the microbubble filled cavity on the myocardial wall imaging quality. Also, using phased arrays and diverging waves instead of linear probes and plane waves allows for a large field of view while avoiding the presence of shadowing. This demands adaptation of the approach notably in terms of motion registration.

- Moreover, the blood motion patterns coming from the ventricular cavity are inconsistent with the motion of the surrounding tissue. The proposed method to counter this effect was to weight the velocity measures according to an autocorrelation-based weighting function, but this implies the smoothing of the cavity coordinates with the surrounding tissue. Our focus being towards the intramyocardial portion of the image, we have targeted to assess this limitation in future works.
- A limitation of this study regarding the analysis of dynamic patterns comes from depicting slow moving microbubbles. As the current state of the framework cannot entirely suppress motion, the slow-moving microbubbles can be filtered with the slow-moving tissue motion of the heart and not taken into the microbubble density maps. Additionally, future works will integrate microbubble tracking algorithms to generate velocity maps of the microvessels to strengthen the dynamic evaluation abilities of this framework.
- A limitation of the Lagrangian coordinates estimation comes from the reduced image quality of using a plane wave imaging framework. According to our calculations, the necessary frame rate to sample speeds of a few tens of cm/s in the rat's heart without aliasing is around 2-3 kHz, which could not be obtained through focused-beam transmissions.
- Additionally, it would be of great interest in future works to evaluate different motion registration methods such as RF-based speckle tracking which was unavailable due to the sampling used in this study.
- The computational cost of MULA is an important factor to mention. The algorithm retrieving the lagrangian coordinates was performed on the first 20 ensembles of 1200 images, requiring a completion time of a few minutes. However, the remaining groups of images were all processed through the Lagrangian beamformer, SVD-based tissue filtering and microbubble localization. These steps required around 1 minute per ensemble to compute, requiring a total computational time of around 13 hours for the processing of the ultrasonic acquisition.
- Segmentation was performed on images formed by using plane wave emissions, which are suboptimal given their relatively low contrast. Sequences including an additional focused Bmode acquisition for segmentation, followed by a high frame rate plane wave acquisition could be used instead.
- The proposed Lagrangian beamformer design depends on manually chosen parameters affecting its performance and limiting of the generalization of MULA to a larger population. The weighting components of regularization terms were chosen by iteration and analysis of results, but it remains challenging to ensure a robust parametrization of the algorithm due to its nature. A quantitative metric should be drawn from the Doppler measurements to assess the validity of the motion field. However, numerous subjects would be required to test this hypothesis and validate its performance.
- Regarding validation of the proposed method, future works will imply the comparison of the generated vascular maps with a gold standard such as the imaging of the microvasculature through micro-CT and a larger sample of subjects.

V. Conclusion

In this study, we have demonstrated the feasibility of Dynamic Myocardial Ultrasound Localization Angiography (MULA) to investigate the angioarchitecture and dynamic behavior of the myocardium's microvasculature in the in vivo beating heart of a rat. To our knowledge, this new method would be a first opportunity to assess these measurements directly, non-invasively and without ionization. With the capability to image a main therapeutic target for coronary artery diseases and coronary microvascular dysfunction, this technique has the potential to lead to novel diagnosis approaches based on the mapping of the microvasculature within the beating heart.

Acknowledgment

The authors would like to thank Marc-Antoine Gillis for his contribution to the experimental procedures.

References

[1] G. B. J. Mancini *et al.*, "Canadian cardiovascular society guidelines for the diagnosis and management of stable ischemic heart disease," *Can. J. Cardiol.*, vol. 30, no. 8, pp. 837–849, Aug. 2014, doi: 10.1016/j.cjca.2014.05.013.

[2] P. A. L. Tonino *et al.*, "Angiographic versus functional severity of coronary artery stenoses in the FAME study," *J. Amer. College Cardiol.*, vol. 55, no. 25, pp. 2816–2821, Jun. 2010, doi: 10.1016/j.jacc.2009.11.096.

[3] D. Garcia *et al.*, "Relationship between FFR, CFR and coronary microvascular resistance—Practical implications for FFR-guided percutaneous coronary intervention," *PLoS ONE*, vol. 14, no. 1, Jan. 2019, Art. no. e0208612, doi: 10.1371/journal.pone.0208612.

[4] P. G. Camici, G. d'Amati, and O. Rimoldi, "Coronary microvascular dysfunction: Mechanisms and functional assessment," *Nature Rev. Cardiol.*, vol. 12, no. 1, pp. 48–62, Jan. 2015, doi: 10.1038/nrcardio.2014.160.

[5] G. Montalescot, "2013 ESC guidelines on the management of stable coronary artery disease: The task force on the management of stable coronary artery disease of the European society of cardiology," *Revista Española de Cardiología*, vol. 67, no. 2, p. 135, Feb. 2014, doi: 10.1016/j.rec.2013.11.008.

[6] B. De Bruyne and J. Sarma, "Fractional flow reserve: A review," *Heart*, vol. 94, no. 7, pp. 949–959, Jul. 2008, doi: 10.1136/hrt.2007.122838.

[7] S. Vijayan, D. S. Barmby, I. R. Pearson, A. G. Davies, S. B. Wheatcroft, and M. Sivananthan, "Assessing coronary blood flow physiology in the cardiac catheterisation laboratory," *Current Cardiol. Rev.*, vol. 13, no. 3, pp. 232–243, Jul. 2017, doi: 10.2174/1573403X13666170525102618.

[8] S. Orde and A. McLean, "Bedside myocardial perfusion assessment with contrast echocardiography," *Crit. Care*, vol. 20, no. 1, p. 58, Dec. 2016, doi: 10.1186/s13054-016-1215-7.

[9] M. Tanter and M. Fink, "Ultrafast imaging in biomedical ultrasound," *IEEE Trans. Ultrason., Ferroelectr., Freq. Control*, vol. 61, no. 1, pp. 102–119, Jan. 2014, doi: 10.1109/TUFFC.2014.2882.

[10] D. Maresca *et al.*, "Noninvasive imaging of the coronary vasculature using ultrafast ultrasound," *JACC, Cardiovascular Imag.*, vol. 11, no. 6, pp. 798–808, Jun. 2018, doi: 10.1016/j.jcmg.2017.05.021.

[11] B.-F. Osmanski, D. Maresca, E. Messas, M. Tanter, and M. Pernot, "Transthoracic ultrafast Doppler imaging of human left ventricular hemodynamic function," *IEEE Trans. Ultrason., Ferroelectr., Freq. Control*, vol. 61, no. 8, pp. 1268–1275, Aug. 2014, doi: 10.1109/TUFFC.2014.3033.

[12] J. Provost *et al.*, "Simultaneous positron emission tomography and ultrafast ultrasound for hybrid molecular, anatomical and functional imaging," *Nature Biomed. Eng.*, vol. 2, no. 2, pp. 85–94, Feb. 2018, doi: 10.1038/s41551-018-0188-z.

[13] M. Correia *et al.*, "Quantitative imaging of coronary flows using 3D ultrafast Doppler coronary angiography," *Phys. Med. Biol.*, vol. 65, no. 10, Jun. 2020, Art. no. 105013, doi: 10.1088/1361-6560/ab8d78.

[14] C. Errico *et al.*, "Ultrafast ultrasound localization microscopy for deep super-resolution vascular imaging," *Nature*, vol. 527, no. 7579, pp. 499–502, Nov. 2015, doi: 10.1038/nature16066.

[15] P. Song *et al.*, "Improved super-resolution ultrasound microvessel imaging with spatiotemporal nonlocal means filtering and bipartite graph-based microbubble tracking," *IEEE Trans. Ultrason., Ferroelectr., Freq. Control*, vol. 65, no. 2, pp. 149–167, Feb. 2018, doi: 10.1109/TUFFC.2017.2778941.

[16] Y. Hao *et al.*, "Non-rigid motion correction for ultrasound localization microscopy of the liver *in vivo*," in *Proc. IEEE Int. Ultrason. Symp. (IUS)*, Glasgow, U.K., Oct. 2019, pp. 2263–2266, doi: 10.1109/ULTSYM.2019.8925749.

[17] M. R. Lowerison, C. Huang, F. Lucien, S. Chen, and P. Song, "Ultrasound localization microscopy of renal tumor xenografts in chicken embryo is correlated to hypoxia," *Sci. Rep.*, vol. 10, no. 1, p. 2478, Dec. 2020, doi: 10.1038/s41598-020-59338-z.

[18] F. Lin, S. E. Shelton, D. Espíndola, J. D. Rojas, G. Pinton, and P. A. Dayton, "3-D ultrasound localization microscopy for identifying microvascular morphology features of tumor angiogenesis at a resolution beyond the diffraction limit of conventional ultrasound," *Theranostics*, vol. 7, no. 1, pp. 196–204, 2017, doi: 10.7150/thno.16899.

[19] O. Couture, V. Hingot, B. Heiles, P. Muleki-Seya, and M. Tanter, "Ultrasound localization microscopy and super-resolution: A state of the art," *IEEE Trans. Ultrason., Ferroelectr., Freq. Control*, vol. 65, no. 8, pp. 1304–1320, Aug. 2018, doi: 10.1109/TUFFC.2018.2850811.

[20] C. Papadacci, E. A. Bunting, E. Y. Wan, P. Nauleau, and E. E. Konofagou, "3D myocardial elastography in Vivo," *IEEE Trans. Med. Imag.*, vol. 36, no. 2, pp. 618–627, Nov. 2016.

[21] C. P. Loizou, C. S. Pattichis, and J. D'hooge, Eds., "Introduction to speckle tracking in cardiac ultrasound imaging," in *Handbook of Speckle Filtering and Tracking in Cardiovascular Ultrasound Imaging and Video*. London, U.K.: IET, 2018, pp. 571–598.

[22] D. Barbosa, B. Heyde, T. Dietenbeck, D. Friboulet, J. D'hooge, and O. Bernard, "Fast left ventricle tracking in 3D echocardiographic data using anatomical affine optical flow," in *Functional Imaging and Modeling of the Heart*, vol. 7945, S. Ourselin, D. Rueckert, and N. Smith, Eds. Berlin, Germany: Springer, 2013, pp. 191–199.

[23] N. Ouzir, A. Basarab, O. Lairez, and J.-Y. Tourneret, "Robust optical flow estimation in cardiac ultrasound images using a sparse representation," *IEEE Trans. Med. Imag.*, vol. 38, no. 3, pp. 741–752, Mar. 2019, doi: 10.1109/TMI.2018.2870947.

[24] C.-M. Yu, J. E. Sanderson, T. H. Marwick, and J. K. Oh, "Tissue Doppler imaging," *J. Amer. College Cardiol.*, vol. 49, no. 19, pp. 1903–1914, May 2007, doi: 10.1016/j.jacc.2007.01.078.

[25] J. Poree, M. Baudet, F. Tournoux, G. Cloutier, and D. Garcia, "A dual tissue-Doppler optical-flow method for speckle tracking echocardiography at high frame rate," *IEEE Trans. Med. Imag.*, vol. 37, no. 9, pp. 2022–2032, Sep. 2018, doi: 10.1109/TMI.2018.2811483.

[26] R. L. Maurice and M. Bertrand, "Lagrangian speckle model and tissue-motion estimation-theory [ultrasonography]," *IEEE Trans. Med. Imag.*, vol. 18, no. 7, pp. 593–603, Jul. 1999.

[27] W.-N. Lee, J. Provost, K. Fujikura, J. Wang, and E. E. Konofagou, "*In vivo* study of myocardial elastography under graded ischemia conditions," *Phys. Med. Biol.*, vol. 56, no. 4, pp. 1155–1172, Feb. 2011, doi: 10.1088/0031-9155/56/4/017.

[28] W.-N. Lee, C. M. Ingrassia, S. D. Fung-Kee-Fung, K. D. Costa, J. W. Holmes, and E. E. Konofagou, "Theoretical quality assessment of myocardial elastography with *in vivo* validation," *IEEE Trans. Ultrason., Ferroelectr., Freq. Control*, vol. 54, no. 11, pp. 2233–2245, Nov. 2007, doi: 10.1109/TUFFC.2007.528.

[29] V. Hingot, C. Errico, M. Tanter, and O. Couture, "Subwavelength motion-correction for ultrafast ultrasound localization microscopy," *Ultrasonics*, vol. 77, pp. 17–21, May 2017, doi: 10.1016/j.ultras.2017.01.008.

[30] G. Montaldo, M. Tanter, J. Bercoff, N. Benech, and M. Fink, "Coherent plane-wave compounding for very high frame rate ultrasonography and transient elastography," *IEEE Trans. Ultrason., Ferroelectr., Freq. Control*, vol. 56, no. 3, pp. 489–506, Mar. 2009, doi: 10.1109/TUFFC.2009.1067.

[31] B. Dunmire, K. W. Beach, K.-H. Labs, M. Plett, and D. E. Strandness, Jr., "Cross-beam vector Doppler ultrasound for angle-independent velocity measurements," *Ultrasound Med. Biol.*, vol. 26, no. 8, pp. 1213–1235, Oct. 2000, doi: 10.1016/S0301-5629(00)00287-8.

[32] C. Kasai, K. Namekawa, A. Koyano, and R. Omoto, "Real-time two-dimensional blood flow imaging using an autocorrelation technique," *IEEE Trans. Sonics Ultrason.*, vol. 32, no. 3, pp. 458–464, May 1985.

[33] F. L. Bookstein, "Principal warps: Thin-plate splines and the decomposition of deformations," *IEEE Trans. Pattern Anal. Mach. Intell.*, vol. 11, no. 6, pp. 567–585, Jun. 1989, doi: 10.1109/34.24792.

[34] T. Shiota, *3D Echocardiography*, 2nd ed. Boca Raton, FL, USA: CRC Press, 2013.

[35] K. C. Assi *et al.*, "Intraventricular vector flow mapping—A Doppler-based regularized problem with automatic model selection," *Phys. Med. Biol.*, vol. 62, no. 17, pp. 7131–7147, Aug. 2017, doi: 10.1088/1361-6560/aa7fe7.